ELSEVIER

Powder Technology 116 (2001) 155–165

POWDER TECHNOLOGY

www.elsevier.com/locate/powtec

Experimental validation of Lagrangian–Eulerian simulations of fluidized beds

B.G.M. van Wachem *, J. van der Schaaf [a], J.C. Schouten [1], R. Krishna [b], C.M. van den Bleek [a]

[a] DelftChemTech, Chemical Reactor Engineering Section, Delft University of Technology, Julianalaan 136, 2628 BL Delft, Netherlands
[b] Department of Chemical Engineering, University of Amsterdam, Nieuwe Achtergracht 166, 1018 WV Amsterdam, Netherlands

Received 1 March 2000; received in revised form 15 June 2000; accepted 16 June 2000

Abstract

The present study aims to validate two-dimensional Lagrangian–Eulerian simulations of gas–solid fluidized beds by comparing these with dedicated experimental data obtained with polystyrene Geldart type D particles of 1.545 mm size.

Experimental data on pressure, voidage, and bed height fluctuations, and the power spectral density are compared with three different implementations of the Lagrangian–Eulerian model. Though qualitative trends found in the experiment are correctly reproduced by the simulations, it is found that the simulations are particularly sensitive to porosity estimation procedures used in the three different simulation strategies employed. Furthermore, the phenomenon of particle clustering predicted by the model does not conform to experimental observations; this is because the physics of the break-up of clusters is not properly captured in the Lagrangian-Eulerian model. © 2001 Elsevier Science B.V. All rights reserved.

Keywords: Gas–solid fluidized beds; Lagrangian simulation; Discrete particles; Pressure fluctuations; Lagrangian–Eulerian framework

1. Introduction

Due to increasing computer power, discrete particle models, or Lagrangian models, have become a very useful and versatile tool to study the hydrodynamic behavior of particulate flows. In these models, the Newtonian equations of motion are solved for each individual particle, and a collision model is applied to handle particle encounters. Recently, such particle models have been combined with a Eulerian fluid model to simulate freely bubbling fluidized beds and circulating fluidized beds (e.g. Refs. [4,12,16]). Up to date, however, these models have not been properly validated by comparison with experiments.

Another approach in simulating the behavior of fluidized beds is through Eulerian–Eulerian modeling. In this approach the particle phase is averaged and thus the particles are not seen as separate objects, as in Jackson [6] (volume averaging) or Zhang and Prosperetti [17] (ensemble averaging). After the correct particle and gas governing equations are obtained, closure relations need to be applied to describe the particle–particle interactions and the gas–particle interactions. The conservation laws applicable during a hard sphere collision are volume averaged to describe the particle–particle interactions. This was done for an ideal gas consisting of fully elastic particles by, for instance, Chapman and Cowling [2]. For more realistic particles, Lun et al. [8] successfully derived the kinetic theory of granular flow (KTGF). This theory provides the particle–particle closure derived from first principles.

The drawback of volume averaging the particle phase, as in the Eulerian–Eulerian approach, is the loss of small-scale information. In the Eulerian–Eulerian approach, it is impossible to predict the paths of individual particles, while Lagrangian models can be used to study the motion of each individual particle. In the Lagrangian–Eulerian approach, in which the paths of individual particles are calculated, many researchers do employ a coarser grid resolution for the gas phase equations than the length-scale that is used in the particle-phase calculations. Hence, the

---

* Corresponding author. Present address: Laboratory of Chemical Reactor Engineering, Eindhoven University of Technology, P.O. Box 513, 5600 MB Eindhoven, The Netherlands. Fax: +31-40-244-6653.
E-mail address: B.G.M.v.Wachem@tue.nl (B.G.M. van Wachem).
[1] Present address: Laboratory of Chemical Reactor Engineering, Eindhoven University of Technology, P.O. Box 513, 5600 MB Eindhoven, The Netherlands.

PII: S0032-5910(00)00389-2

gas-phase does not perceive, initiate, group, or break-up particle clusters when the clusters are smaller than the length scale of the gas-phase solution. As a result, micro-scale cluster formation is not driven by gas flow, but only by particle–particle collisions. Also, due to the different averaging scales, the gas does not flow around small clusters of particles, but flows through them as if the clusters are a fixed porous medium. Only when clustering is mainly initiated by particle–particle collisions and clusters are much larger than the gas-phase averaging scale, the use of a coarser gas-phase grid resolution is justified.

The goal of this work is to validate the predictions of the Lagrangian–Eulerian model with experiments of a small fluidized bed with Geldart D particles, to gain insight in the effect of the assumptions made in the Lagrangian–Eulerian model derivation. The small bed geometry and the large particles make the computationally expensive Lagrangian–Eulerian simulations of this system feasible. Results obtained from simulations of the pressure fluctuations, voidage fluctuations, bed expansion, and the visual representation of the location of the particles are compared to experiments with the same geometry, particle type, and superficial gas velocities.

2. Particle phase

We consider flows of homogeneous, inelastic, frictional spheres in a two-dimensional geometry. The path of each individual particle is calculated, this is called a Lagrangian calculation. The calculation of the paths of the particles consists of two steps: (i) calculating the motion of the particles, and (ii) the treatment of the collision of a particle with another particle.

2.1. Motion of particles

The motion of individual particles is completely determined by Newton's second law of motion. The forces acting on each particle are gravity and the traction force of the gas phase on the particle. Thus, the momentum equation describing the acceleration of the particle is [6]

$$m_\mathrm{s}\mathbf{a}_\mathrm{s} = m_\mathrm{s}g + V_\mathrm{s}\nabla\cdot\bar{\bar{\tau}} - V_\mathrm{s}\nabla P + \beta\frac{V_\mathrm{s}}{\epsilon_\mathrm{s}}(\mathbf{v}_\mathrm{g}-\mathbf{v}_\mathrm{s}) \tag{1}$$

where $\mathbf{a}_\mathrm{s}$ is the acceleration of one particle, V_s is the volume of one particle, $\bar{\bar{\tau}}$ is the local gas phase shear tensor, P is the local normal pressure, ϵ_s is the local solid volume fraction, and β represents the interphase momentum exchange coefficient, as is well-known from two-fluid models. The gas phase shear tensor is defined as

$$\bar{\bar{\tau}} = 2\mu\bar{\bar{D}} - \frac{2}{3}\mu\,\mathrm{tr}(\bar{\bar{D}})\bar{\bar{I}} \tag{2}$$

where $\bar{\bar{D}}$ is the strain rate tensor,

$$\bar{\bar{D}} = \frac{1}{2}\left(\nabla\mathbf{v} + (\nabla\mathbf{v})^\mathrm{T}\right) \tag{3}$$

and μ the gas-phase viscosity. In most cases, the magnitude of the gas-phase shear tensor is not significant and its contribution can be safely omitted, as it is an order of magnitude smaller than the pressure drop.

Xu and Yu [16] omit the pressure drop term in their particle phase momentum equation. From our simulations, we have seen that this pressure drop term, however, is not negligible but of the same order of magnitude as the interphase momentum transfer coefficient.

Wen and Yu [15] have performed settling experiments of solid particles in a liquid over a wide range of solid volume fractions and have correlated their data and that of others for solids concentrations of $0.01 \leq \epsilon_\mathrm{s} \leq 0.63$. The interphase momentum transfer coefficient β is given by Wen and Yu [15] as

$$\beta = \frac{3}{4}C_\mathrm{D}\frac{(1-\epsilon_\mathrm{s})\epsilon_\mathrm{s}\rho_\mathrm{g}|\mathbf{v}_\mathrm{g}-\mathbf{v}_\mathrm{s}|}{d_\mathrm{p}}(1-\epsilon_\mathrm{s})^{-2.65} \tag{4}$$

with the drag coefficient C_D given by Rowe [11] as

$$C_\mathrm{D} = \begin{cases} \dfrac{24}{Re_\mathrm{p}(1-\epsilon_\mathrm{s})}\left[1+0.15((1-\epsilon_\mathrm{s})Re_\mathrm{p})^{0.687}\right] & \text{if } (1-\epsilon_\mathrm{s})Re_\mathrm{p} < 1000 \\ 0.44 & \text{if } (1-\epsilon_\mathrm{s})Re_\mathrm{p} \geq 1000 \end{cases} \tag{5}$$

where the particle Reynolds number Re_p is defined as

$$Re_\mathrm{p} = \frac{d_\mathrm{p}\rho_\mathrm{g}|\mathbf{v}_\mathrm{g}-\mathbf{v}_\mathrm{s}|}{\mu_\mathrm{g}} \tag{6}$$

The interaction of the particle rotation with the gas-phase is neglected. This assumption is verified in the Results section.

2.2. Collision of particles

The collisions between two particles are assumed binary, and the velocities of the particles emerging from a collision are calculated by considering the balance of linear and angular momenta in the collision. The simplified model proposed by Louge [7], originally developed by Maw et al. [9], is employed to describe the dynamics of individual collisions. During a collision, energy is stored in elastic deformations associated with both the normal and the tangential displacements of the contact point relative to the center of the sphere. Because the release of this energy may affect the rebound significantly, coefficients of restitution associated with both the normal and tangential components of the velocity point of contact are taken into account. This model is employed for both particle–particle and particle–wall collisions.

We consider two colliding spheres with diameters d_1 and d_2 with masses m_1 and m_2 with centers located at $\mathbf{r}_1$ and $\mathbf{r}_2$. The unit normal along the line joining the centers of two spheres is $\mathbf{n} = (\mathbf{r}_1 - \mathbf{r}_2)/|\mathbf{r}_1 - \mathbf{r}_2|$. During the collision, sphere 2 exerts an impulse $\mathbf{J}$ onto sphere 1. Prior to the collision the spheres have translational velocities $\mathbf{c}_1$ and $\mathbf{c}_2$ and angular velocities $\boldsymbol{\omega}_1$ and $\boldsymbol{\omega}_2$. The corresponding velocities after the collision are denoted by primes. The velocities before and after collision are related by

$$m_1(\mathbf{c}'_1 - \mathbf{c}_1) = -m_2(\mathbf{c}'_2 - \mathbf{c}_2) = \mathbf{J} \tag{7}$$

and

$$\frac{2I_1}{d_1}(\boldsymbol{\omega}'_1 - \boldsymbol{\omega}_1) = -\frac{2I_2}{d_2}(\boldsymbol{\omega}'_2 - \boldsymbol{\omega}_2) = -\mathbf{n} \times \mathbf{J} \tag{8}$$

where $I = md^2/10$ is the moment of inertia about the center of a homogeneous sphere. In order to determine the impulse $\mathbf{J}$, the relative velocity $\mathbf{q}$ at the point of contact is defined:

$$\mathbf{q} = (\mathbf{c}_1 - \mathbf{c}_2) - \left(\frac{d_1}{2}\boldsymbol{\omega}_1 + \frac{d_2}{2}\boldsymbol{\omega}_2\right) \times \mathbf{n} \tag{9}$$

With the above equations, the contact velocities before and after the collision are given by

$$\mathbf{q}' - \mathbf{q} = \frac{7}{2}\left(\frac{1}{m_1} + \frac{1}{m_2}\right)\mathbf{J} - \frac{5}{2}\left(\frac{1}{m_1} + \frac{1}{m_2}\right)\mathbf{n}(\mathbf{J} \cdot \mathbf{n}) \tag{10}$$

The coefficient of restitution, e, characterizes the incomplete restitution of the normal component of $\mathbf{q}$:

$$\mathbf{n} \cdot \mathbf{q}' = -e\mathbf{n} \cdot \mathbf{q} \tag{11}$$

where $0 \le e \le 1$. In collisions that involve sliding, the sliding is assumed to be resisted by Coulomb friction and the tangential and normal components of the impulse are related by the coefficient of friction μ:

$$|\mathbf{n} \times \mathbf{J}| = \mu(\mathbf{n} \cdot \mathbf{J}) \tag{12}$$

where $\mu \ge 0$. Combining Eqs. (10)–(12) provides an expression for the impulse transfer in the case when the collision is sliding:

$$\mathbf{J}^{(1)} = \frac{(1+e)(\mathbf{q} \cdot \mathbf{n})\mathbf{n} + \mu(1+e)\cot\gamma[\mathbf{q} - \mathbf{n}(\mathbf{q} \cdot \mathbf{n})]}{\left(\frac{1}{m_1} + \frac{1}{m_2}\right)} \tag{13}$$

where γ is the angle between $\mathbf{q}$ and $\mathbf{n}$ and the superscript 1 denotes that the collision involves sliding. With small γ the collision is sliding, and as γ increases the sliding stops when

$$\mathbf{n} \times \mathbf{q}' = -\xi\mathbf{n} \times \mathbf{q} \tag{14}$$

or equivalently

$$\cot\gamma_0 = \frac{2(1+\xi)}{7(1+e)\mu} \tag{15}$$

where $0 \le \xi \le 1$ is the tangential coefficient of restitution. Collisions with $\gamma \ge \gamma_0$ do not involve sliding but sticking, and in this case the impulse is found by combining (Eqs. (10), (11) and (14):

$$\mathbf{J}^{(2)} = -\frac{(1+e)(\mathbf{q} \cdot \mathbf{n})\mathbf{n} + \frac{2}{7}(1+\xi)[\mathbf{q} - \mathbf{n}(\mathbf{q} \cdot \mathbf{n})]}{\left(\frac{1}{m_1} + \frac{1}{m_2}\right)} \tag{16}$$

In this expression, the superscript 2 denotes the collision does not involve sliding, but sticking. The three parameters e, μ, and ξ are taken to be constant and independent of the velocities.

Collisions with a flat wall are treated by considering the wall as a particle with infinite mass and with the appropriate wall values of e, μ, and ξ.

2.3. From two dimensions to three dimensions

If the local porosity, ϵ_g, is calculated by dividing the void space (not occupied by particles) by the total space, this will give a different result in two dimensions and in three dimensions. To correct for this inconsistency, Hoomans et al. [4] suggest to transform the two-dimensional porosity with the following equation:

$$\epsilon_{3D} = 1 - \frac{2}{\sqrt{\pi\sqrt{3}}}(1 - \epsilon_{2D})^{\frac{3}{2}} \tag{17}$$

where ϵ_{2D} is the porosity defined as the area occupied by disks in the two-dimensional space. The basis of this equation is to assume equal spacing between the two-dimensional disks in a hexagonal lattice and three-dimensional particles in a FCC lattice. Xu and Yu [16] propose a different equation,

$$\epsilon_{3D} = 1 - \frac{\sum_{i=1}^{K} V_i}{\Delta V} \tag{18}$$

in which the summation is taken over all the particles in the volume ΔV, which is the volume of a computational cell with the thickness of one particle, thus $\Delta V = \Delta x \Delta y d_p$, and V_i is the volume of particle i. This equation gives slightly different predictions for ϵ_{3D} than the equation proposed by Hoomans et al. [4].

Because of the ideal spherical particles in the two-dimensional simulations, the ideal solids packing can be easily obtained. In practice, however, this packing is never obtained. A third method should also be considered, namely the one proposed by Hoomans et al. [4], but now we have introduced an empirical parameter containing the maximum experimental solids packing in practice, ν, thus

$$\epsilon_{3\mathrm{D}} = 1 - \nu \frac{2}{\sqrt{\pi\sqrt{3}}} \left(1 - \epsilon_{2\mathrm{D}}\right)^{\frac{3}{2}} \tag{19}$$

$$\nu = \frac{1 - \epsilon_{3\mathrm{D,\,experimental\,minimum}}}{1 - \epsilon_{3\mathrm{D,\,theoretical\,minimum}}} \tag{20}$$

Both the Eqs. (17) and (19) are used in this work and the results of simulations employing both expressions are compared with each other.

A fundamental problem regarding the translation of the corresponding number of particles in two-dimensions to the number of particles in three-dimensions is the pressure drop. When the two-dimensional bed is filled with particles up to a certain height, the number of two-dimensional particles is not equal to the number of particles as experienced by the gas-phase, due to the translation of the voidage from two-dimensions to three-dimensions. Hence, the pressure drop calculated in the gas-phase is less than the weight of the particles, by the pre-factor in Eq. (17). Thus, the pressure drop calculated by two-dimensional Lagrangian simulations will predict too low a pressure drop compared to experiments with the same initial bed height. Increasing the number of particles to correct for this loss of weight will increase the pressure drop, but will also change the dynamics of the particle phase because the height-over-diameter ratio of the dense fluidized bed is changed. Both of the mentioned strategies are employed in this paper.

3. Gas phase

The motion of the gas-phase is calculated from the volume averaged gas-phase governing equations as put forward by Jackson [6]. The continuity equation for the gas phase is

$$\frac{\partial \epsilon_{\mathrm{g}} \rho_{\mathrm{g}}}{\partial t} + \nabla \cdot \epsilon_{\mathrm{g}} \mathbf{v}_{\mathrm{g}} = 0 \tag{21}$$

and the momentum balance is

$$\begin{aligned} &\frac{\partial \epsilon_{\mathrm{g}} \rho_{\mathrm{g}} \mathbf{v}_{\mathrm{g}}}{\partial t} + \nabla \cdot \left(\epsilon_{\mathrm{g}} \rho_{\mathrm{g}} \mathbf{v}_{\mathrm{g}} \mathbf{v}_{\mathrm{g}} \right) \\ &\quad = -\epsilon_{\mathrm{g}} \nabla P + \epsilon_{\mathrm{g}} \nabla \cdot \bar{\bar{\tau}}_{\mathrm{g}} + \epsilon_{\mathrm{g}} \rho_{\mathrm{g}} \mathbf{g} \\ &\qquad - \sum_{i=1}^{K} \frac{V_{\mathrm{s},i} \beta \left(\mathbf{v}_{\mathrm{g}} - \mathbf{v}_{\mathrm{s},i} \right)}{\epsilon_{\mathrm{s}}} \delta \left(\mathbf{x} - \mathbf{x}_{\mathrm{s},i} \right) \end{aligned} \tag{22}$$

in which the last term represents the interphase momentum transfer between the gas phase and each individual particle. δ represents a pulse function, which is one if its argument is zero and zero otherwise. The last term is to ensure that the interphase momentum transfer is only taken into account in the gas-phase momentum equation at the location of the corresponding particle.

The left and right walls of the fluidized bed are treated as no-slip velocity boundary conditions for the gas-phase. Dirichlet boundary conditions are employed at the bottom with a uniform gas inlet velocity. The boundary condition at the top the fluidized bed is a so-called pressure boundary. The pressure at this boundary is fixed to a reference value, $1.013 \cdot 10^5$ Pa, and Neumann boundary conditions are applied to the gas-phase velocity, requiring a fully-developed gas flow.

As was indicated earlier, a problem of this Lagrangian–Eulerian approach is the length-scale of the averaging. In the Eulerian–Eulerian approach the length scales of the averaged gas-phase and particle-phase are equal and the “sub-grid” behavior of the particles is described with the kinetic theory of granular flow. In the Lagrangian–Eulerian approach, the length-scale of the gas-phase is larger than the length-scale of the particle phase. The information of gas induced movement of particles, as well as particle-induced movement of gas, cannot be transferred between the phases on the eddy or individual particle scale. Hence, a computational cell in which a small cluster of particles is present is penetrated by the gas-phase, similar as a fixed porous medium; the gas phase does not discriminate between homogeneously distributed particles or clustered particles within one cell. In reality, the gas-phase “dodges” the particle cluster and moves perpendicular to the initial flow before the cluster. Particle clustering due to the local gas flow (“micro-scale” clustering) is thus not captured in the Lagrangian–Eulerian approach. This treatment of the particle-gas phase coupling should be well kept in mind when attempting to use this simulation method.

4. Solution method

The gas-phase is calculated on a computational grid with individual grid size of four to eight particle diameters. The gas-phase governing equations have been solved on a staggered grid (e.g. Ref. [10]) employing the SIMPLE algorithm to determine the pressure of the gas phase. The discretization of the terms is done with a second order TVD scheme in space and the second-order Crank–Nicholson scheme in time. A preconditioned bi-conjugent gradient method was employed to solve the discretized gas-phase equations.

The solid volume fraction in the gas-phase momentum equation is determined from the number of particles in the gas-phase computational cell, by employing Eq. (17). The interphase momentum transfer is calculated from the last term of the gas-phase momentum balance, and this coupling is treated explicitly. To justify this explicit coupling, the chosen time-step must be smaller than the time-scale of the gas–particle interaction. We have found $\Delta t \approx 1.0 \cdot 10^{-4}$ s to be satisfactory; the particle motion due to the gas-phase does not depend upon the size of the timestep. The gas-phase properties at the particle surface are calculated by area weighted averaging, as shown in Fig. 1. This method is not mesh-size independent, as there is a direct coupling between average particle properties, such as particle porosity and velocity, and the gas-phase. The mesh-size of the gas-phase needs to be small enough to predict realistic gas–particle interactions, and large enough to determine an accurate average value for the particle porosity, momentum transfer, and velocity. We have found that the length of one gas-phase grid cell should be in the order of 4 to 10 particle diameters.

After initialization of both phases, first the shortest collision time of each particle is determined. This is done by comparing the location and velocity of each particle with the other particles in the near vicinity by using a particle-phase mesh, without checking a pair of particles twice, as indicated by Fig. 2. The collision time between two particles is determined by Allen and Tildesley [1] as

$$t_{\mathrm{col}} = \frac{-\mathbf{r}_{12}\cdot\mathbf{c}_{12} - \sqrt{(\mathbf{r}_{12}\cdot\mathbf{c}_{12})^2 - c_{12}^2\left[r_{12}^2 - \left(\frac{1}{2}d_1 + \frac{1}{2}d_2\right)^2\right]}}{c_{12}^2} \tag{23}$$

where $\mathbf{r}_{12} \equiv \mathbf{r}_1 - \mathbf{r}_2$ and $\mathbf{c}_{12} \equiv \mathbf{c}_1 - \mathbf{c}_2$. If the inproduct $\mathbf{r}_{12} \cdot \mathbf{c}_{12} > 0$, the particles are moving away from each other and will not collide. If the overall shortest collision time (of all the particles) is larger than the time-step of the gas-phase calculation, the particle positions are updated by the integration of Eq. (1) with the same time-step as the gas-phase. Hereafter, the gas-phase properties are computed and the forces exerted by the gas phase on each individual particle are calculated. Now, the shortest collision times are determined again and the process is repeated from the beginning.

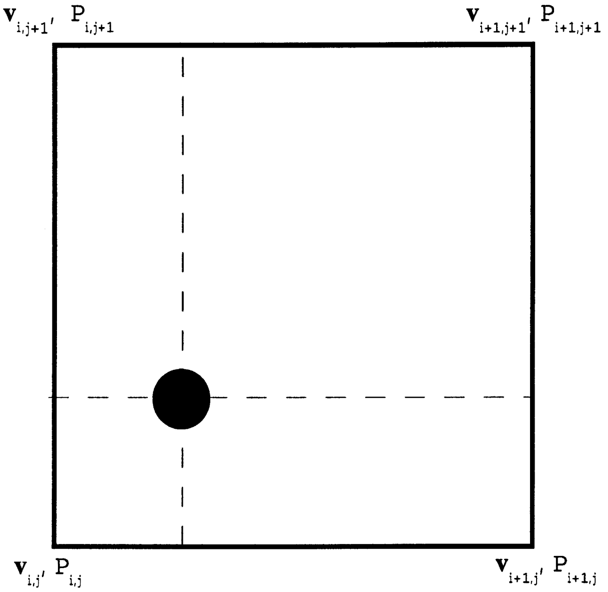

Fig. 1. The principle of area weighted averaging. The gas-phase properties are given in the corners of the gas-phase cell by the gas-phase solution and are averaged to the center of the particle (denoted by the black dot) by using the overlying areas as weighting factors. This figure has been adapted from Hoomans et al. [4].

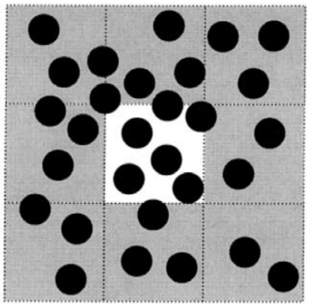

Fig. 2. A three-by-three particle mesh. The shortest times of collision of the particles in the center cell are determined by comparing the locations and velocities of the particles in the white center cell with all the particles in the nine particle cells. For the calculation times in the next particle cell, comparing the particles in that cell with the particles in the white cell is no longer necessary.

If the overall shortest collision time is smaller than the time-step of the gas-phase, the particle positions are updated by this shortest overall collision time. Hereafter, the collision of the two particles in question is executed. Then again, the shortest collision times of all particles are calculated. This is repeated, until the overall shortest collision time is shorter than the time-step of the gas-phase calculation minus the time-steps of all previous collisions during this iteration. When the overall shortest collision time is larger than the time remaining until the end of the gas-phase time-step, the gas-phase is updated. This process is repeated until the required real time of simulation is obtained.

5. Experiments and simulations

5.1. Experimental set-up

The experimental set-up consisted of a two-dimensional plexiglass rectangular column, 500 mm high, 90 mm wide, and 8 mm deep. A schematic representation of the set-up is given in Fig. 3. The gas flow was controlled with a variable area flow meter and a valve. The dry air from the compressor system was humidified to reduce static electricity build-up in the fluidized bed. The gas was only humidified partially to prevent condensation of water in the bed (operating temperature 17°C); polystyrene spheres with a density of 1150 kg m^{-3} and a diameter of 1.54 mm

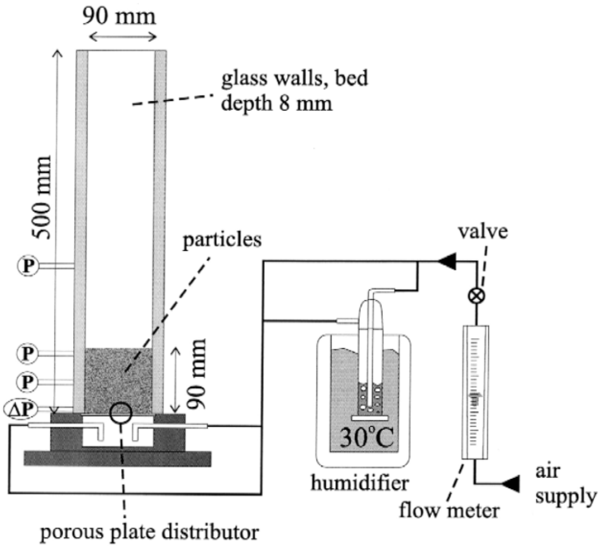

Fig. 3. The experimental set-up employed in this work. The symbols P indicate where the pressure signals are determined.

(1.41–1.68 mm sieve fraction) were used as particle system. The bed was filled to a height of 90 mm, corresponding to 39 g of particles, which leads to a packed bed voidage of 0.475. The minimum fluidization velocity calculated using Ergun's equation is 0.74 m/s, agreeing quite well with the experimentally determined value of 0.72 m/s. The experiments were carried out at superficial gas velocities of $U = 0.80$ m/s, $U = 0.90$ m/s, and $U = 1.0$ m/s.

5.2. Measurements

Absolute pressure fluctuations were measured with Kistler piezo electric pressure transducers, type 7261 at the side of the bed at heights of 45, 85, and 225 mm from the distributor plate. This sensor type measures the pressure fluctuation relative to the average pressure with an accuracy of 2 Pa. The sensors were connected to 0.10 m long copper tubes of 4 mm ID, the total dead volume of sensor and tube was 2500 mm^3. The tubes were equipped with 40 μm mesh wire gauze at the tips, to prevent particles from entering. This set-up has been thoroughly tested for distortion of pressure fluctuation amplitude and phase [13]. No significant influence was found at frequencies typical for gas–solids fluidized beds (0–150 Hz). Also, the absolute pressure was measured with a Validyne differential pressure transducer, type DP15, at a height of 5 mm. For each time-series, 300,032 data points were recorded to file with 16 bits ADC using a SCADAS II data acquisition system (LMS, Breda, The Netherlands). The sample frequency was set to 1000 Hz with a filter frequency of 314 Hz. The time-series were analyzed using Fourier analysis and compared to the simulations. In addition to pressure measurements, digital video recordings (25 frames/s, 60 s long) of the fluidized bed were made and analyzed. The local voidage was calculated, from the light intensity determined by the video recording, using the Lambert–Beer relation,

$$\epsilon_s = -\frac{1}{a}\ln\left(\frac{I}{I_0}\right) \tag{24}$$

where I is the measured light intensity, I_0 is the minimum light intensity, and a is obtained from calibration of the measured light-intensity and the corresponding known solids concentration.

5.3. Simulations

As explained earlier, there are several ways of determining the number of particles which need to be used in a two-dimensional simulation in order to be able to mimic the experiments. The solids volume fraction in the two-dimensional configuration at the minimum fluidization velocity can be determined by transforming the measured solids volume fraction with Eq. (17) to the appropriate two-dimensional solids volume fraction. When the width–height aspect ratio of the fluidized bed is equal to the experiments, this approach leads to 3110 required particles. When the ideal two-dimensional maximum solids volume fraction is used, the number of required particles is 4080. Both these strategies are employed in this paper. The particle specifications used in the simulations are the same as in the experiments. The empirical parameter in the equation to translate the porosity from two dimensions to three dimensions, Eq. (19), is determined experimentally to be $\nu = 0.89$. For the coefficient of restitution and coefficient of friction, generally proposed values were employed. The details of the simulation conditions are specified in Table 1. Both the simulations and the experiments were carried out at superficial gas velocities of $U = 0.8$ m/s, $U = 0.9$ m/s, and $U = 1.0$ m/s.

Three different simulation strategies were followed. In strategy A, the equation of Hoomans et al. [4] is employed

Table 1
Properties of the particles and fluidized bed used in the experiments and the Lagrangian–Eulerian simulations

Parameter	Description	Value
ρ_s [kg/m^3]	solid density	1150
ρ_g [kg/m^3]	gas density	1.28
μ_g [Pa s]	gas viscosity	$1.7 \cdot 10^{-5}$
d_p [mm]	particle diameter	1.545
e [–]	coefficient of restitution	0.9
μ [–]	coefficient of friction	0.3
U_{mf} [m/s]	minimum fluidization velocity	0.74
D_T [m]	column width	0.0898
H_{mf} [m]	height at minimum fluidization	0.09
$\epsilon_{s,mf}$ [–]	solids volume fraction at minimum fluidization	0.525
ν [–]	empirical parameter in Eq. (19)	0.89
Δx [m]	x mesh spacing	$9.97 \cdot 10^{-3}$
Δy [m]	y mesh spacing	$9.97 \cdot 10^{-3}$

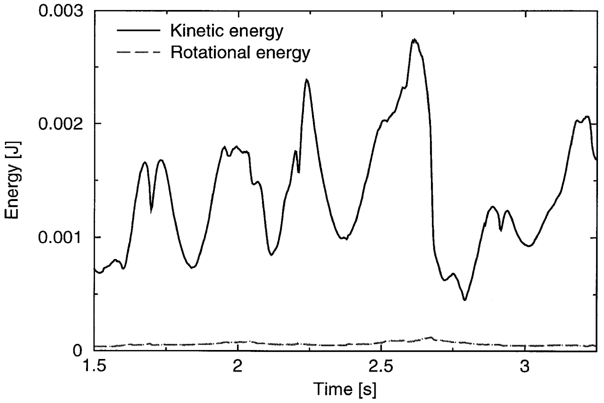

Fig. 4. The total kinetic energy and rotational energy as a function of time predicted by a simulation of a fluidized bed with a superficial gas velocity $U = 0.9$ m/s.

to translate the two-dimensional porosity into a three-dimensional one. The simulations with this strategy contain 3110 particles. In strategy B, the fit equation (Eq. (19)) to translate the porosity from two dimensions to three dimensions is employed. Simulations with this strategy also contain 3110 particles. Strategy C employs the Hoomans et al. [4] equation to translate the two-dimensional porosity to a three-dimensional one, and the simulations following this strategy contain 4080 particles, to ensure the correct bed height at zero superficial gas velocity (absent gas-phase), because then the two-dimensional particles are ideally packed.

Fig. 4 shows the kinetic energy and the rotational energy as a function of time. The average rotational energy is an order of magnitude smaller than the average kinetic energy. Hence, rotational effects, including influence of particle rotation on the gas-phase, can be safely neglected.

5.4. Comparison

The locations of all the particles in the simulations of the fluidized bed are qualitatively compared to the digital video recordings made of the fluidized bed at the same operating conditions. More quantitatively, the simulation predictions of the total time-averaged pressure drop over the fluidized bed, the pressure fluctuations at 45 mm above the distributor, the average voidage fluctuations in a plane at 45 mm above the distributor, and the time-dependent bed expansion are compared with experiments employing the same operating conditions. Furthermore, the power spectral densities (PSD) of the simulated pressure fluctua-

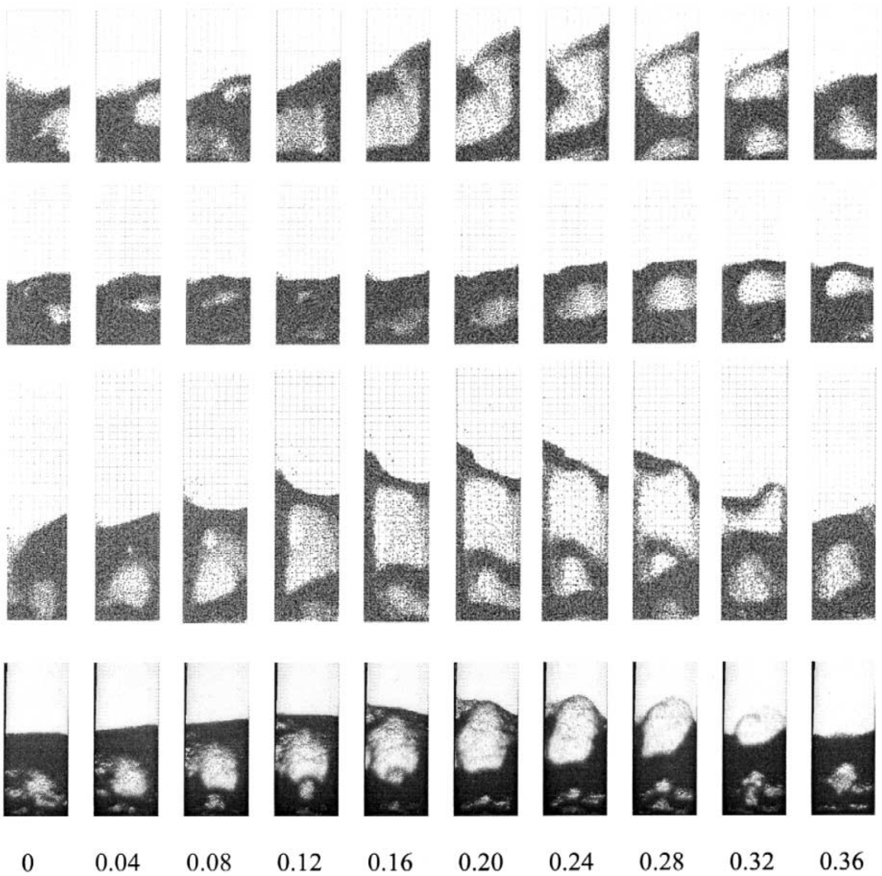

Fig. 5. Ten snapshots of a visual representation of the location of the particles at equidistant times (given at the bottom of the series in seconds) at a superficial gas velocity of $U = 0.9$ m/s. The top series represents a simulation employing strategy A, the second series is a result of strategy B, and the third series is a result of employing strategy C. The bottom series are snapshots of the experiment taken by a video camera.

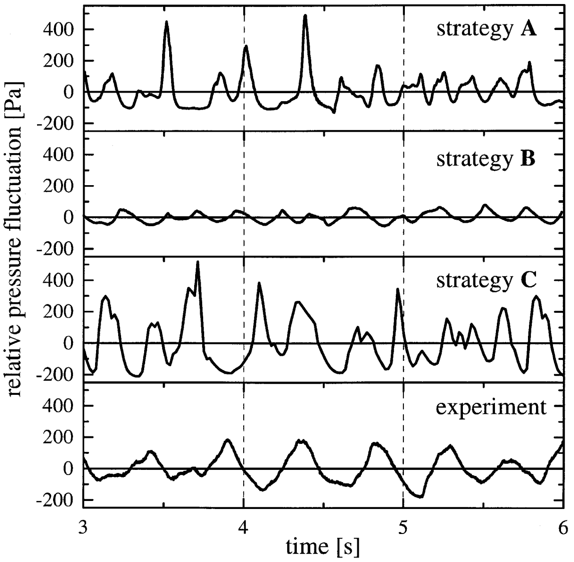

Fig. 6. Pressure fluctuation samples taken at $U = 0.9$ m/s at 45 mm above the distributor, resulting from the three simulation strategies compared to the experiment.

tions are compared with the experimentally determined predicted fluctuations.

6. Results and discussion

Fig. 5 shows a visual comparison of the location of the particles in three simulations at a superficial gas velocity at $U = 0.9$ m/s and snapshots from the corresponding experiment covering a complete period from bubble formation to bubble eruption. Animations of the performed experiments and simulations can be viewed at the WWW address http://www.tcp.chem.tue.nl/ ~ scr/wachem/particle.html.

In all three simulation strategies employed, large clusters of particles were found to be present at the top of the bubble during bubble eruption. This phenomenon is not observed in the experiments. The simulated particle clusters are too stable, which is attributed to the Lagrangian–Eulerian approach, as discussed earlier. The top series of snapshots in Fig. 5 represents the simulation as a result of employing strategy A. The period of bed oscillation from bubble formation to bubble eruption of the simulation is visually in fair agreement with the experiment. The second series represents a simulation as a result of employing strategy B. Although the bed oscillation is similar to the one observed in the experiment, the bubble dynamics are not. Due to the extra decreased mass effect because of the fit parameter in Eq. (19), the gas-phase experiences too little resistance from the particle phase. The third series represents a simulation as a result of employing strategy C. The bubble eruption of this series gives a too high bed height compared with the experiment, because the height of the simulated fluidized bed is larger than employed in the experiment. The agreement of the time between bubble formation and bubble eruption of the comparison between all simulations and the experiments is reasonable. Comparison of the simulations and experiments at superficial gas velocities of $U = 0.8$ m/s and $U = 1.0$ m/s show similar results.

The pressure drop in the simulations with 3110 particles is lower (strategy A 340 Pa, strategy B 300 Pa) than the pressure drop measured in the experiments (480 Pa). The predicted pressure drop by the simulation applying strategy C is in very good agreement (483 Pa) with the experiment.

Fig. 6 shows a comparison of a sample of the pressure fluctuation time-series determined at 45 mm above the distributor at $U = 0.9$ m/s. In strategy A, the shape and amplitude of the pressure fluctuations deviate clearly from the experiment; the maximum amplitudes are higher and the peaks are sharper. This suggests that the gas voids in the simulation are larger. The time-scale of the pressure fluctuations is in fairly good agreement with the experiment.

The shape and time-scale of the pressure fluctuations obtained by following strategy B are in reasonable agreement with the pressure fluctuations determined in the experiment; the amplitude of the fluctuations, however, is much smaller. This suggests that in the simulation voids are much smaller than observed in the experiment, confirmed by the visual observations of Fig. 5. The time-scale of the pressure fluctuations obtained from simulations following strategy C agrees reasonably with the experimentally determined pressure fluctuations, but the amplitude is much too high. This suggests that the voids in this simulation are much larger than observed in the experiment. Also the shape of the fluctuations is somewhat different compared to the experimentally determined pres-

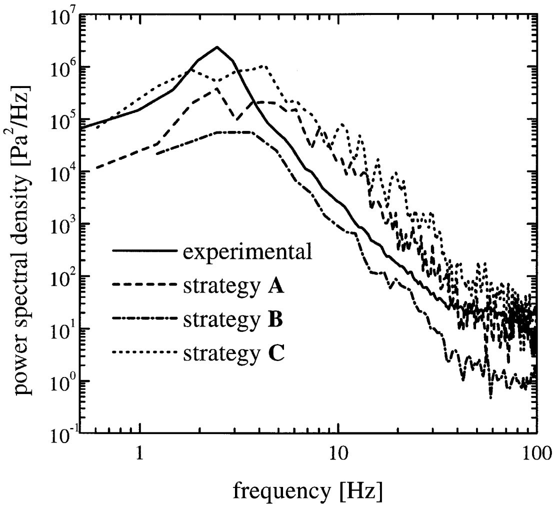

Fig. 7. The power spectral density (PSD) as a function of frequency of the pressure fluctuation series at 45 mm above the distributor at $U = 0.9$ m/s, resulting from the three simulation strategies compared to the experiment.

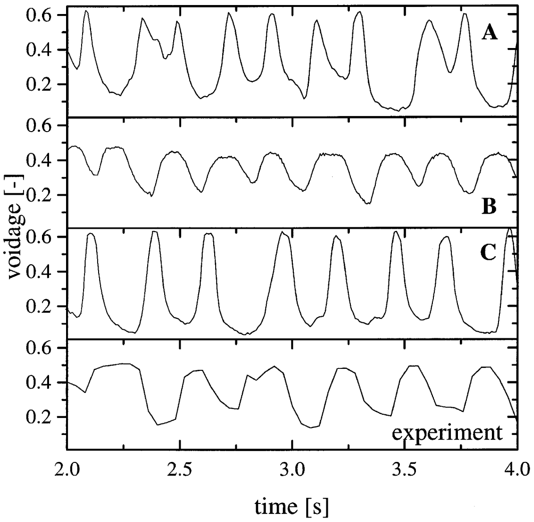

Fig. 8. Fluctuations of the solids volume fraction averaged in a horizontal plane at 45 mm above the distributor at $U = 0.9$ m/s, as a function of time, resulting from the three simulation strategies compared to the experiment.

sure fluctuations. Pressure fluctuations obtained at different heights show very similar results.

The power spectral densities (PSD) of the complete pressure fluctuating time-series determined at $U = 0.9$ m/s at 45 mm above the distributor are shown in Fig. 7. This figure shows that the location of the dominant frequency at approximately 3 Hz, imposed by the bubble behavior, is similar in the experiment and in all the simulations. This figure confirms that this most dominant frequency is less pronounced in the simulations than in the experiment, denoted by the more broad maxima in the PSD of the simulations at the most dominant frequency. The decrease in the PSD curve in Fig. 7 at frequencies exceeding 5 Hz, a power law fall-off, is a typical feature of gas–solid fluidized beds [14]; the agreement between experiment and simulations is remarkably good on this point.

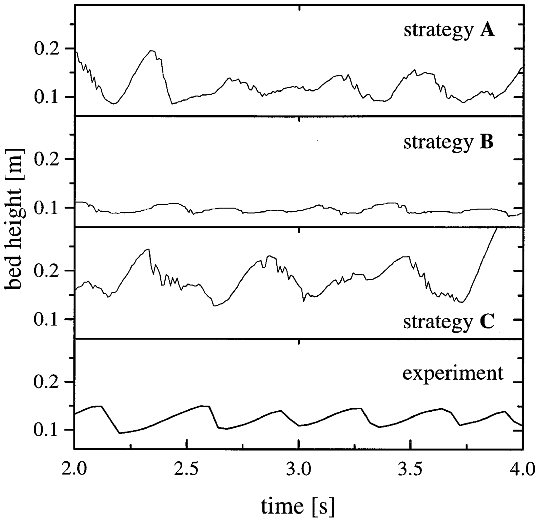

Fig. 9. Fluctuations of the bed height at $U = 0.9$ m/s, as a function of time, resulting from the three simulation strategies compared to the experiment.

Table 2
The average bed expansion and the standard deviation determined for the three simulation strategies and the experiment

Gas velocity	0.8 m/s	0.9 m/s	1.0 m/s
Strategy	Bed expansion [m]		
A	0.119 ± 0.021	0.124 ± 0.027	0.146 ± 0.332
B	0.094 ± 0.003	0.097 ± 0.008	0.104 ± 0.180
C	0.162 ± 0.041	0.190 ± 0.046	0.212 ± 0.298
experiment	0.114 ± 0.009	0.120 ± 0.019	0.138 ± 0.019

Fig. 8 shows the voidage fluctuations, as a function of time, averaged in a horizontal plane at 45 mm above the distributor, at $U = 0.9$ m/s, of the three simulation strategies in comparison with the experiment. Simulated voidage fluctuations as a result of strategies A and C show too large fluctuations and also the shape of the fluctuations is too sharp in comparison with the experiment. This also suggests that the voids present in the simulations following strategies A and C are too large. Simulations performed with strategy B show shapes and amplitudes that are much more similar to the measured voidage fluctuations. All three simulation strategies predict a slightly too small time-scale of the voidage fluctuations.

Fig. 9 shows the bed height as a function of time as a result of the three simulation strategies and the experiment at $U = 0.9$ m/s. All simulation strategies show quite different results compared to the experiment. The average time-scale of the bed fluctuation is in fairly good agreement, which can also be seen from Fig. 5. The amplitudes of the bed expansion in simulations by strategy A and C are too large. This is a result of too vigorous bubbling, indicating larger gas voids than present in the experiments. The bed expansion amplitude from simulations following strategy B is too small. Enlarging the empirical factor ν in Eq. (19) will improve the results, as this translation equation will then produce results closer to strategies A and C.

The average bed expansion and its standard deviation for the three simulation strategies and the experiment are shown in Table 2. Strategy A compares well to the experiment; it seems that the increase in void size, due to the interphase-momentum transfer equation, is accounted for by the number of particles.

7. Conclusions

The goal of this paper is to validate two-dimensional Lagrangian–Eulerian simulations of a gas–solid fluidized bed containing polystyrene particles with laboratory-scale experiments of the same geometry. One difficulty in the two-dimensional Lagrangian–Eulerian model is the translation of the two-dimensional porosity of the particles to a three-dimensional one, required by the gas-phase and the interphase momentum transfer. To tackle this problem, we have followed three strategies, A, B, and C, in performing simulations, each with different assumptions. In one of the strategies, we have included an empirical parameter to fine-tune the pressure drop or the bed expansion with the experimentally determined one. We have not found a strategy, however, that can successfully predict all features of the fluidized bed as observed in the experiments. Performing three-dimensional Lagrangian simulations either with a two-dimensional or three-dimensional Eulerian gas-phase will overcome the difficulty in translating the two-dimensional porosity to a three-dimensional one, but will increase the computational cost as the number of particles to obtain the required bed height in three-dimensions is much larger than in two-dimensions.

Because the gas-phase hydrodynamics are resolved on a larger scale than the particle-phase dynamics, the method is not grid independent and “micro-scale” clustering cannot be captured. Animations show that “micro-scale” clustering does contribute to the total fluidized bed behaviour. Resolving the gas phase on a scale smaller than the particle size, either by direct numerical simulation (DNS) [5] or by the more elegant fictitious domain method [3], can resolve this problem.

Overall, the two-dimensional Lagrangian–Eulerian simulations are in fair agreement with the experiments. With an added empirical parameter in the translation from the two-dimensional porosity to the three-dimensional porosity the pressure drop or the bed expansion can be fine-tuned. To capture the behaviour of the physics of the fluidized bed more precisely, applying a three-dimensional Lagrangian–Eulerian method is advised.

Nomenclature

a	empirical parameter
$\mathbf{a}$	particle acceleration, m s^{-2}
$\mathbf{c}$	particle velocity, m s^{-1}
C_D	drag coefficient
d_p	particle diameter, m
D_T	column width, m
$\overline{\overline{D}}_s$	strain rate tensor, s^{-1}
e	coefficient of restitution
$\mathbf{g}$	gravitational constant, m s^{-2}
H	height, m
I	moment of inertia, kg m^2
J	impulse transfer during collision, kg m s^{-1}
K	number of particles
L	light intensity, cd
m	particle mass, kg
$\mathbf{n}$	normal vector, m
P	pressure, Pa
q	relative velocity, m s^{-1}
Re	Reynolds number
$\mathbf{r}$	point in space, m
t	time, s
U	inlet (superficial) gas velocity, m s^{-1}
U_{mf}	minimum fluidization velocity, m s^{-1}
$\mathbf{v}$	velocity vector, m s^{-1}
ΔV	volume of computational cell, m^3
V_s	particle volume m^3
Δx	x mesh spacing, m
Δy	y mesh spacing, m

Greek

β	interphase drag constant, kg m^{-3} s^{-1}
γ	angle between impact and normal
ϵ	volume fraction
μ	friction coefficient
ν	empirical parameter, Eqs. (19) and (20)
ρ	density, kg m^{-3}
$\bar{\bar{\tau}}$	viscous stress tensor, N m^{-2}
ξ	tangential coefficient of restitution

Subscript

0	minimum intensity
1,2	particle index
2D	two-dimensional
3D	three-dimensional
g	gas phase
mf	at minimum fluidization
p	particle
s	solids phase

Acknowledgements

These investigations were supported (in part) with financial assistance from the Netherlands Organization for Scientific Research (NWO). This support is gratefully acknowledged.

References

[1] M.P. Allen, D.J. Tildesley, Computer Simulation of Liquids, Oxford Univ. Press, Oxford, 1980.

[2] S. Chapman, T.G. Cowling, The Mathematical Theory of Non-Uniform Gases, 3rd edn., Cambridge Univ. Press, 1970.

[3] R. Glowinski, T.-W. Pan, T.I. Hesla, D.D. Jospeh, A distributed lagrange multiplier/fictitious domain method for particulate flows, Int. J. Multiphase Flow 25 (1999) 755–794.

[4] B.P.B. Hoomans, J.A.M. Kuipers, W.J. Briels, W.P.M. van Swaaij, Discrete particle simulation of bubble and slug formation in a two-dimensional gas-fluidised bed: a hard-sphere approach, Chem. Eng. Sci. 51 (1) (1996) 99–118.

[5] H.H. Hu, Direct simulation of flows of solid–liquid mixtures, Int. J. Multiphase Flow 22 (2) (1996) 335–352.

[6] R. Jackson, Locally averaged equations of motion for a mixture of identical spherical particles and a newtonian fluid, Chem. Eng. Sci. 52 (1997) 2457–2469.

[7] M.Y. Louge, Computer simulations of rapid granular flows of spheres interacting with a flat, frictional boundary, Phys. Fluids 6 (1994) 2253–2269.

[8] C.K.K. Lun, S.B. Savage, D.J. Jefferey, N. Chepurniy, Kinetic theories for granular flow: inelastic particles in couette flow and slightly inelastic particles in a general flowfield, J. Fluid Mech. 140 (1984) 223–256.

[9] N. Maw, J.R. Barber, J.N. Fawcett, The oblique impact of elastic spheres, Wear 38 (1976) 101–114.

[10] S.V. Patankar, Numerical Heat Transfer and Fluid Flow, Hemisphere Publising, London, 1980.

[11] P.N. Rowe, Drag forces in a hydraulic model of a fluidized bed, part II, Trans. Inst. Chem. Eng. 39 (1961) 175–180.

[12] Y. Tsuji, T. Kawaguchi, T. Tanaka, Discrete particle simulation of two-dimensional fluidized bed, Powder Technol. 77 (1993) 79–87.

[13] J.R. van Ommen, J.C. Schouten, M.L.M. vander Stappen, C.M. van den Bleek, Response characteristics of probe-transducer systems for pressure measurements in gas–solid fluidized beds: how to prevent pitfalls in dynamic pressure measurements, Powder Technol. 106 (1999) 199–218.

[14] B.G.M. van Wachem, J.C. Schouten, R. Krishna, C.M. Van den Bleek, Validation of the Eulerian simulated dynamic behaviour of gas–solid fluidised beds, Chem. Eng. Sci. 54 (1999) 2141–2149.

[15] C.Y. Wen, Y.H. Yu, Mechanics of fluidization, Chem. Eng. Progr. Symp. Ser. 62 (1966) 100–111.

[16] B.H. Xu, A.B. Yu, Numerical simulation of the gas–solid flow in a fluidized bed by combining discrete particle method with computational fluid dynamics, Chem. Eng. Sci. 52 (16) (1997) 2785–2809.

[17] D.Z. Zhang, A. Prosperetti, Averaged equations for inviscid disperse two-phase flow, J. Fluid Mech. 267 (1994) 185–219.